Understanding the Physical Degrees of Freedom in a Parameterized Test of General Relativity

Leif Lui [1, 2, *] Rico K. L. Lo [2, †] and Alan J. Weinstein [2, ‡]

[1] *Department of Physics, The Chinese University of Hong Kong, Sha Tin, NT, Hong*
[2] *LIGO, California Institute of Technology, Pasadena, California 91125, USA*

(Dated: August 27, 2021)

This paper provides a framework for understanding the physical degrees of freedom in a parameterized test of general relativity. In particular, we vary the post-Newtonian (PN) coefficients, the phenomenological coefficients, and the analytical black-hole perturbation theory waveform parameters, and observe how this would affect the waveform and hence the physical parameters. The physical parameters include the energy radiated and the rate of angular momentum. Although it is possible to map the dephasing coefficients to physical quantities, the inverse mapping of the physical quantities to the dephasing coefficients is unknown. Therefore, this paper presents a method of obtaining this inverse mapping using the Gaussian Mixture Model (GMM).

I. INTRODUCTION

The detection of gravitational waves (GWs) by the Advanced LIGO and Virgo [1–11] has opened new windows in observational astrophysics and cosmology. More specifically, it stands to test the limits of Einstein's theory of general relativity (GR). More recent work has been focused on testing GR in the strong-field/highly-relativistic regime. Such tests could potentially reconcile the deviations of GR with quantum field theory, through examining the higher-energy corrections to the Einstein-Hilbert action [12].

Of the many strong-field astrophysical events, this paper focuses on the coalescence of binary black holes (BBHs). This is because, firstly, the gravitational fields generated can be many orders of magnitude stronger than any other astrophysical event, as the BBHs' orbital separation can be smaller than the last stable orbit before merging. Secondly, BBH coalescence gives one of the cleanest signals for testing GR, as it is separated into three distinct phases: the inspiral, merger, and ringdown (IMR) phases [13].

A parametrized test is where one measures the deviation of some parameters from their GR predictions. For parameterized tests of GR, the phenomenological models are most ideal, as they have a closed-form expression in the frequency domain and hence can be more computationally efficient. In particular, we focus on doing a parameterized test of GR on `IMRPhenomPv2` [14–17]. `IMRPhenomPv2` is a waveform model that approximates a signal of a precessing binary. It is used because it has good performance across the parameter space [15]. For details see Appendix. The purpose of the parameterized test is to understand the physical significance of varying the dephasing coefficients in the waveform and see whether such changes have deviations from GR.

Throughout the entirety of this paper, the geometric unit convention is adopted, where $c = G = 1$.

II. THEORY

A. Parameterized Test of GR

As mentioned in the Section I, a parameterized test of GR is to search for deviations of observations from the predictions of GR. To perform the parameterized tests, we introduce fractional deviations δp_i to the `IMRPhenomPv2` phase coefficients p_i [18], namely

$$p_i \to (1 + \delta p_i) p_i. \tag{1}$$

These fractional deviations are known as the dephasing coefficients. The phasing of `IMRPhenomPv2` consists of three regimes. The first of which is the inspiral regime which is parameterized by post-Newtonian (PN) coefficients [19] $\{\chi_0, \ldots, \chi_7\}$ and $\{\chi_{5l}, \chi_{6l}\}$. In this regime, there are also phenomenological parameters $\{\sigma_0, \ldots, \sigma_4\}$ that contribute to the high effective PN order. This corrects for non-adiabaticity in the late inspiral phase and unknown high-order PN coefficients in the adiabatic regime. The second regime, is the intermediate regime, which is parameterized by the phenomenological coefficients $\{\beta_0, \ldots, \beta_3\}$. Finally, there is the merger-ringdown regime which is parameterized by a combination of the phenomenological coefficients and the analytical black-hole perturbation theory parameters $\{\alpha_0, \ldots, \alpha_5\}$ [13]. As one can see if $\delta p_i = 0$ this corresponds to a theory with no deviation from GR.

In FIG. 1, we have the phase evolution of an `IMRPhenomPv2` waveform with varied dephasing coefficients. A dephasing coefficient is chosen from each regime to illustrate how the dephasing coefficient changes the waveform and hence the physical parameters. More specifically, FIG. 1 illustrates how the dephasing coefficient changes the phase. In FIG. 2, we change the same dephasing coefficients as those in FIG. 1, however this time we plotted the strain data. This illustrates how the

* leif.lui@ligo.org
† ka-lok.lo@ligo.org
‡ alan.weinstein@ligo.org

dephasing coefficient changes the shape of the GW waveform. Note that, the deviations of dephasing coefficients in FIG. 1 and FIG. 2 have been exaggerated to make the deviations more visible. Such high deviations have been ruled out with observations [1, 14, 20].

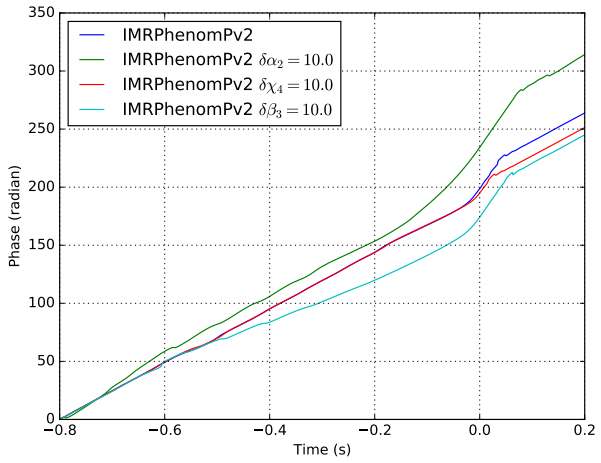

FIG. 1. Phase of GW versus time for `IMRPhenomPv2` with no modification (blue line), $\delta\alpha_2 = 10.0$ (orange line), $\delta\chi_4 = 10.0$ (green line), and $\delta\beta_3 = 10.0$ (red line).

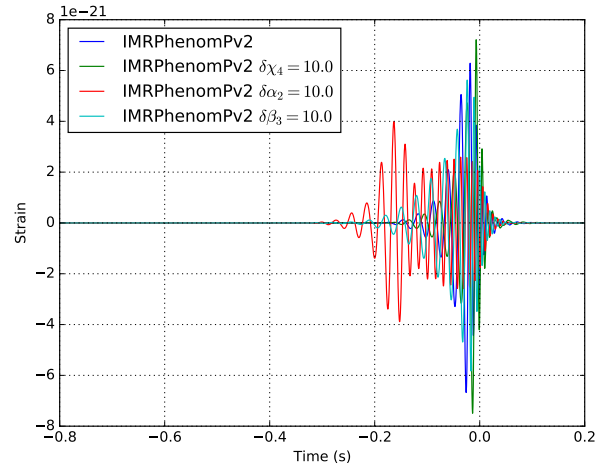

FIG. 2. Strain versus time for `IMRPhenomPv2` with no modification (blue line), $\delta\alpha_2 = 10.0$ (orange line), $\delta\chi_4 = 10.0$ (green line), and $\delta\beta_3 = 10.0$ (red line).

Throughout the entirety of this project, we will use the parameterized test of TIGER (Test Infrastructure for GEneral Relativity) [21, 22]. This infrastructure is preferred, as it is a theory-agnostic test of GR. This means that the infrastructure does not require an alternative theory of gravity to compare against. In addition to this, TIGER is dependent on the measurement of parameterizable deviations, like the aforementioned deviation in dephasing coefficients from a GR-consistent waveform model.

Let $\mathcal{H}_{\rm GR}$ be the hypothesis that some GW signal h is consistent with GR. To test how this hypothesis deviates from GR, we introduce another hypothesis $\mathcal{H}_{\rm MG}$ (MG stands for modified gravity) which is a hypothesis that the waveform model differs by one or more dephasing coefficients. Since $\mathcal{H}_{\rm GR}$ and $\mathcal{H}_{\rm MG}$ are mutually exclusive, and given some data d and information I, we can define the Bayes factor [13]

$$\mathcal{B} = \frac{p(d|\mathcal{H}_{\rm MG}, I)}{p(d|\mathcal{H}_{\rm GR}, I)}, \tag{2}$$

where $p(d|\mathcal{H}_{\rm GR}, I)$ and $p(d|\mathcal{H}_{\rm MG}, I)$ are the posterior probability densities of the data given hypotheses $\mathcal{H}_{\rm GR}$ and $\mathcal{H}_{\rm MG}$, respectively. If $\log \mathcal{B} > 0$, then the hypothesis $\mathcal{H}_{\rm MG}$ is favored, on the other hand if $\log \mathcal{B} < 0$ the hypothesis $\mathcal{H}_{\rm GR}$ is preferred [23]. Hence, we have a quantitative way of determining whether a waveform deviates from GR. This can be computed using some Bayesian inference software packages like `bilby` [24] or `LALInference` [25, 26].

B. Parameter Estimation

In Ref. [13], the Bayesian statistics framework is used to do parameter estimation. In such framework, the posterior distribution for some parameter λ is [13, 25, 26]

$$p(\lambda|\mathcal{H}_i, d, I) = \frac{p(\lambda|\mathcal{H}_i, I)p(d|\mathcal{H}_i, \lambda, I)}{p(d|I)}, \tag{3}$$

where $\mathcal{H}_i$ is the hypothesis that corresponds to a waveform model in which δp_i is a free parameter. In Eq. (3), d is the data, I is the background information, $p(\lambda|\mathcal{H}_i, I)$ is the prior probability density for the free parameters, and $p(d|\mathcal{H}_i, \lambda, I)$ is the probability of the data. $p(d|\mathcal{H}_i, \lambda, I)$ is defined as the likelihood function, which can be written as [13, 25, 26]

$$p(d|\mathcal{H}_i, \lambda, I) \propto e^{-\frac{1}{2}\langle d-h(\lambda)|d-h(\lambda)\rangle}, \tag{4}$$

where $h(\lambda)$ is the signal model and the inner product is defined as [13]

$$\langle a|b\rangle = 4\Re \int_{f_{\rm low}}^{f_{\rm high}} {\rm d}f \frac{a^*(f)b(f)}{S_n(f)}. \tag{5}$$

In Eq. (5), $f_{\rm high}$ is the high-frequency cutoff and $f_{\rm low}$ is the low-frequency cutoff. In the equation above, $S_n(f)$ is the power spectral density of noise. To obtain the posterior density for parameter δp_i, one has to marginalize over all parameters other than δp_i. These are also known as the nuisance parameters.

$$p(\delta p|\mathcal{H}_i, d, I) = \int {\rm d}\vec{\theta}\, p(\vec{\theta}, \delta p_i|\mathcal{H}_i, d, I), \tag{6}$$

where the integration is carried out over all nuisance parameters.

C. Rates of Energy and Angular Momentum of GWs

The physical parameters that we are interested in are the rates of energy and angular momentum. We can compute the energy and momentum using the Isaacson stress-energy tensor [27, 28]

$$t_{\mu\nu} = -\frac{1}{8\pi}\left\langle R^{(2)}_{\mu\nu} - \frac{1}{2}\bar{g}_{\mu\nu}R^{(2)}\right\rangle, \tag{7}$$

where $R^{(2)}_{\mu\nu}$ is the Ricci tensor to quadratic order. $R^{(2)}_{\mu\nu}$ usually involves many terms quadratic in the metric perturbation, however we can drastically simplify this expression by performing integration by parts and using the transverse-traceless (TT) gauge condition

$$R^{(2)}_{\mu\nu} = -\frac{1}{4}\left\langle \partial_\mu h_{\alpha\beta}\partial_\nu h^{\alpha\beta}\right\rangle. \tag{8}$$

Therefore the Isaacson stress-energy tensor can be written explicitly as

$$t_{\mu\nu} = \frac{1}{32\pi}\left\langle \partial_\mu h^{\rm TT}_{\alpha\beta}\partial_\nu h^{\alpha\beta}_{\rm TT}\right\rangle. \tag{9}$$

To compute the energy carried by a GW, we take the 00-component of the Isaacson stress-energy tensor and integrate over the volume V [27, 28]

$$\frac{{\rm d}E}{{\rm d}t} = \lim_{r\to\infty}\frac{1}{16\pi}\int_S {\rm d}\Omega\, r^2\left\langle \dot{h}_+^2 + \dot{h}_\times^2\right\rangle, \tag{10}$$

where h_+ and $h_\times$ are the plus and cross polarizations of the GW, respectively. The overhead dot in Eq. (10) is the derivative with respect to coordinate time. Another useful expression is the energy spectrum, as it is much easier to integrate over all frequencies

$$\frac{{\rm d}E}{{\rm d}f} = \lim_{r\to\infty}\frac{\pi}{2}f^2\int_S {\rm d}\Omega\, r^2\left(|\tilde{h}_+(f)|^2 + |\tilde{h}_\times(f)|^2\right). \tag{11}$$

On the other hand, to compute the rate of angular momentum, we compute the linear momentum and take the cross product with the separation vector. The linear momentum is as follows [27, 28]

$$\frac{{\rm d}P_i}{{\rm d}t} = \lim_{r\to\infty}\frac{1}{32\pi}\int {\rm d}\Omega\, r^2\left\langle \dot{h}^{\rm TT}_{ij}\partial^k\dot{h}^{\rm TT}_{ij}\right\rangle. \tag{12}$$

Therefore, the total rate of change in angular momentum carried by the GWs can be written as

$$J^i = \frac{1}{2}\epsilon^{ijk}J_{kl}, \tag{13}$$

where J_{kl} is the conserved charge associated with rotation in the $kl-$plane. Using Noether's theorem, we find that the expression for rate of angular momentum is as follows [27, 28]

$$\frac{{\rm d}J_i}{{\rm d}t} = \lim_{r\to\infty}\frac{1}{32\pi}\int_S {\rm d}\Omega\, r^2\langle -\epsilon^{ikl}\dot{h}^{\rm TT}_{ab}x^k\partial^l h^{\rm TT}_{ab} + 2\epsilon^{ikl}\dot{h}^{\rm TT}_{al}h^{\rm TT}_{ak}\rangle. \tag{14}$$

To carry out the integration, multipole expansion is performed on the rates of energy and angular momentum [28].

D. A Multipole Expansion of Energy

In Eq. (10), h_+ and $h_\times$ are dependent on t, the orbital phase ϕ, and the angle between the angular momentum $\vec{J}$ and line of sight $\hat{n}$, namely θ. To obtain an analytic expression for the integral over solid angle Ω, we separate h_+ and $h_\times$ into a time-dependent part and an angular part. This can be done using spin-weighted spherical harmonics ${}_sY_{\ell m}$. For outgoing GWs, we are concerned with the spin $s=-2$ [28],

$$\begin{aligned} h_+ - ih_\times &= \sum_{l,m} {}_{-2}Y_{lm}(\theta,\phi)h_{l,m}(t) \\ &\approx {}_{-2}Y_{22}(\theta,\phi)h_{2,2}(t) + {}_{-2}Y_{2-2}(\theta,\phi)h_{2,-2}(t), \end{aligned} \tag{15}$$

where the second line has been truncated, because for aligned-spin binaries, the $h_{2,2}$ and $h_{2,-2}$ modes are the leading order terms. Taking the time derivative of Eq. (15) and multiplying this expression by its complex conjugate, we obtain the following expression

$$\begin{aligned} \dot{h}_+^2 + \dot{h}_\times^2 =& |{}_{-2}Y_{22}|^2|\dot{h}_{2,2}|^2 + {}_{-2}Y_{22}\ {}_{-2}Y^*_{2-2}\dot{h}_{2,2}\dot{h}^*_{2,-2} \\ &+ {}_{-2}Y^*_{22}\ {}_{-2}Y_{2-2}\dot{h}^*_{2,2}\dot{h}_{2,-2} + |{}_{-2}Y_{2-2}|^2|\dot{h}_{2,-2}|^2. \end{aligned} \tag{16}$$

With this, the task at hand is to calculate $h_{2,2}$ and $h_{2,-2}$. To do so, we first need to determine the spin-weighted spherical harmonics. Using the Wigner D matrix, ${}_{-2}Y_{22}$ and ${}_2Y_{22}$ in the θ and ϕ representation is as follows

$${}_{-2}Y_{22}(\theta,\phi) = \sqrt{\frac{5}{64\pi}}(1+\cos\theta)^2 e^{2i\phi}, \tag{17}$$

$${}_{-2}Y_{2-2}(\theta,\phi) = \sqrt{\frac{5}{64\pi}}(1-\cos\theta)^2 e^{-2i\phi}. \tag{18}$$

Notice that ${}_{-2}Y_{22}(0,0) = {}_{-2}Y_{2-2}(0,\pi) = \frac{1}{2}\sqrt{\frac{5}{\pi}}$ and ${}_{-2}Y_{2-2}(0,0) = {}_{-2}Y_{22}(0,\pi) = 0$. Therefore, to solve for $h_{2,2}$ and $h_{2,-2}$, we simply calculate $h_+ - ih_\times$ at $\theta=\phi=0$, and $\phi=0$, $\theta=\pi$. This can be done using `PyCBC` and `LALSimulation`. Doing so we find that

$$h_{2,2}(t) = \sqrt{\frac{4\pi}{5}}[h_+(t,0,0) - ih_\times(t,0,0)], \tag{19}$$

and

$$h_{2,-2}(t) = \sqrt{\frac{4\pi}{5}}[h_+(t,\pi,0) - ih_\times(t,\pi,0)]. \tag{20}$$

Since we are considering non-precessing binaries, θ contain no time dependence. Therefore, to integrate Eq.

(15) over solid angle, we simply compute the following integrals,

$$\int_S \mathrm{d}\Omega \, |{}_{-2}Y_{22}|^2 = \int_S \mathrm{d}\Omega \, |{}_{-2}Y_{2-2}|^2 = 1, \tag{21}$$

and

$$\int_S \mathrm{d}\Omega \, {}_{-2}Y^*_{22} \, {}_{-2}Y_{2-2} = \int_S \mathrm{d}\Omega \, {}_{-2}Y_{22} \, {}_{-2}Y^*_{2-2} = \frac{1}{6}. \tag{22}$$

Using the results from Eq. (21) and Eq. (22), we can integrate Eq. (16) over solid angle to obtain the instantaneous power

$$\begin{aligned}\frac{\mathrm{d}E}{\mathrm{d}t} = \lim_{r\to\infty} \frac{r^2}{16\pi} \Big\langle |\dot{h}_{2,2}|^2 + |\dot{h}_{2,-2}|^2 \\ + \frac{1}{6}\left(\dot{h}^*_{2,2}\dot{h}_{2,-2} + \dot{h}_{2,2}\dot{h}^*_{2,-2}\right)\Big\rangle .\end{aligned} \tag{23}$$

III. RESULTS

A. Effects of Varying the Intrinsic Parameters

To calculate $\dot{h}_{2,2}$, $\dot{h}_{2,-2}$, $\dot{h}^*_{2,2}$, and $\dot{h}^*_{2,-2}$, we use numerical methods. More specifically, we use the central difference method to calculate the time derivatives of the arrays. The algorithm for the central difference method is as follows [29]

$$f'(x) \approx \frac{f(x + \frac{1}{2}\delta) - f(x - \frac{1}{2}\delta)}{2\delta}, \tag{24}$$

where f is the function for which the derivative is taken with respect to variable x, and δ is the step size. The central difference method is comparatively more accurate than the forward and backward difference methods. This is because, the forward and backward difference methods have truncation errors of order $\mathcal{O}(\delta)$, whereas the central difference method has a truncation error of order $\mathcal{O}(\delta^2)$ [29].

After computing $\dot{h}_{2,2}$, $\dot{h}_{2,-2}$, $\dot{h}^*_{2,2}$, and $\dot{h}^*_{2,-2}$, we have obtained the instantaneous power. To better depict the evolution of energy over time, we use the cumulative trapezoidal method to numerically calculate the integral of power over time, namely the cumulative energy. The algorithm for the cumulative trapezoidal rule is as follows [30]

$$\int_a^b f(x)dx \approx \sum_{k=1}^{N} \frac{f(x_{k-1}) + f(x_k)}{2} \Delta x_k, \tag{25}$$

where f is the function being integrated with respect to variable x over the interval $[a, b]$, $\{x_k\}$ is the partition of $[a, b]$ such that $a = x_0 < x_1 < \cdots < x_{N-1} < x_N = b$, and $\Delta x_k = x_k + x_{k-1}$ is the kth sub interval [30]. The cumulative trapezoidal rule is used because the algorithm is much simpler to implement in code. There are indeed more accurate methods of obtaining the cumulative energy, however given a large number of data points, the cumulative trapezoidal rule yields sufficiently accurate results for calculating the integral. This can be seen in FIG. 3-5, as the energy versus time graph yields somewhat smooth functions. From here, we vary the intrinsic physical parameters and see how the energy evolves over time. Given the primary and secondary masses of a binary system, namely m_1 and m_2, respectively, the intrinsic parameters we are concern with are: the total mass $M = m_1 + m_2$, the mass ratio $q = \frac{m_2}{m_1}$, and the spins in the z-direction associated with m_1 and m_2, namely s_{1z} and s_{2z}, respectively. We choose $f_{\text{lower}} = 10$ Hz and $f_{\text{high}} = 4096$ Hz, to include the whole waveform.

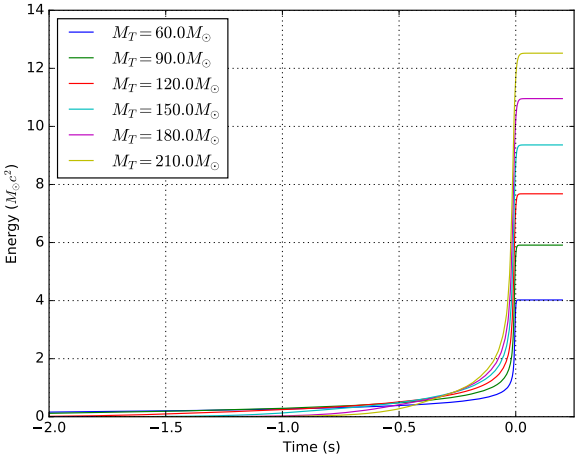

FIG. 3. The radiated energy of GW versus time in linear scale for `IMRPhenomPv2` with constant mass ratio $q = 1.00$ and varying total mass.

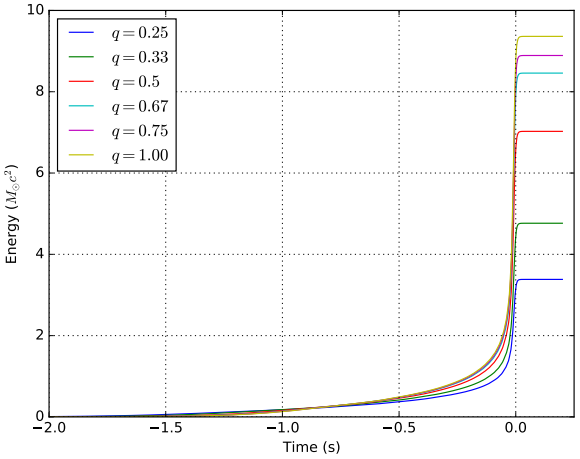

FIG. 4. The radiated energy of GW versus time in linear scale for `IMRPhenomPv2` with varying mass ratio and constant total mass of $M = 150\ M_\odot$.

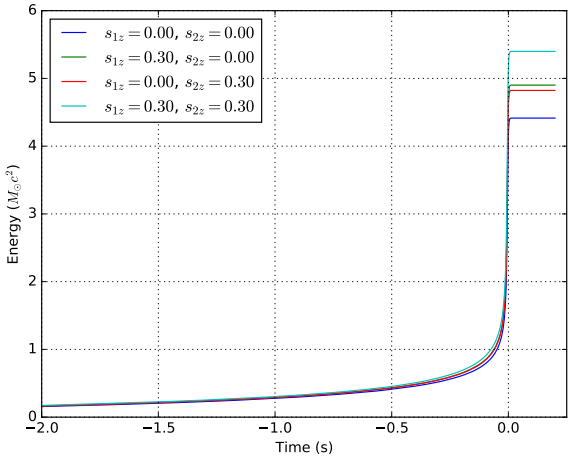

FIG. 5. The radiated energy of GW versus time in linear scale for `IMRPhenomPv2` with varying spin. Here, $m_1 = 35.0\ M_\odot$ and $m_2 = 31.5\ M_\odot$.

In FIG. 3-5 the energy has been plotted for $-2.00 \leq t \leq 0.25$. The graph has been truncated to more clearly illustrate the change in energy during the intermediate and merger-ringdown phase. As seen from FIG. 3-5, the total mass M, the mass ratio q, and spins s_{1z}, s_{2z}, increases with the radiated energy of the GW. From FIG. 3-5, it is also apparent that a change in total mass M, mass ratio q, and spins s_{1z} and s_{2z}, has a major effect on the cumulative energy in the intermediate phase and the merger-ringdown phase. However, more interestingly, it seems that the variation of cumulative energy in the inspiral phase has little to no variation when plotting the cumulative energy versus time graph. To better illustrate the change in energy during the inspiral phase, we plot the y-axis of FIG. 3-5 in logarithmic scale.

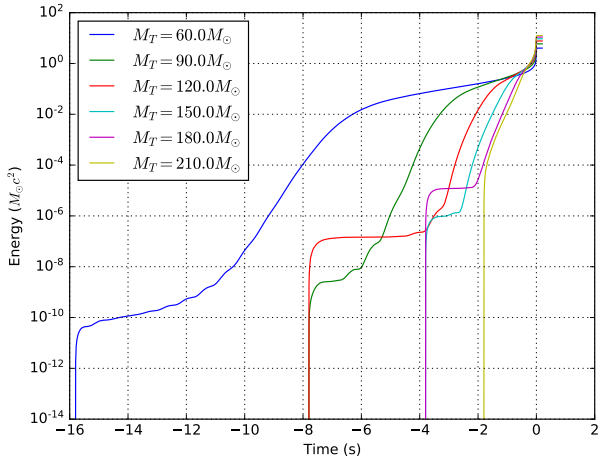

FIG. 6. The radiated energy of GW versus time for `IMRPhenomPv2` with constant mass ratio $q = 1.00$ and varying total mass in logarithmic scale.

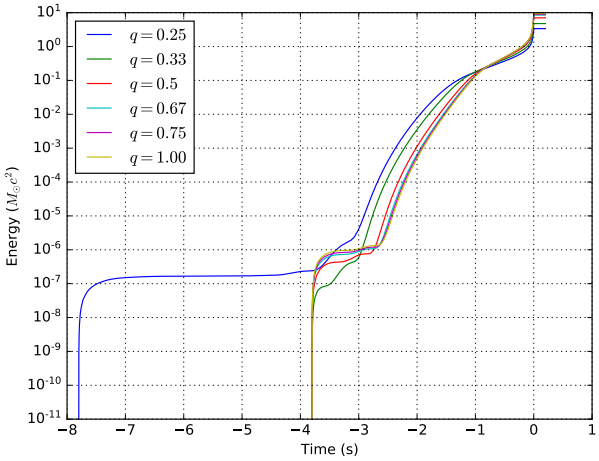

FIG. 7. The radiated energy of GW versus time for `IMRPhenomPv2` with varying mass ratio and constant total mass of $M = 150\ M_\odot$ in logarithmic scale.

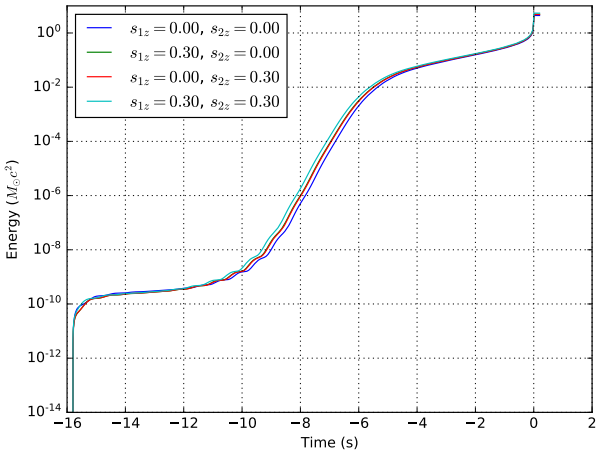

FIG. 8. The radiated energy of GW versus time for `IMRPhenomPv2` with varying spin in logarithmic scale. Here, $m_1 = 35.0\ M_\odot$ and $m_2 = 31.5\ M_\odot$.

From FIG. 6-8, we can see that during the inspiral phase there are small deviations in the total energy radiated by the GW. In FIG. 6, during times $-16.0\ \text{s} \leq t \leq\sim 0.8\ \text{s}$, we can see that the total energy radiated decreases with the total mass. This has an opposite correlation to that of the merger-ringdown phase, as indicated in FIG. 3, where the total mass increases with the GW energy. In FIG. 7, for times $t < -0.13$ s, we can see that the total energy radiated decreases with the mass ratio. Again, this has an opposite correlation to that of the merger-ringdown phase, as indicated in FIG. 4, where the mass ratio increases with the GW energy. In FIG. 8, we can see that at times $t < -0.35$ s, the total energy decreases with the spin. Once more, this has an opposite correla-

tion to that of the merger-ringdown phase, as indicated in FIG. 5, where the spin increases with the GW energy.

B. Effects of Varying the Dephasing Coefficients

The goal in this subsection is to see how the energy evolves over time with varying dephasing coefficients. The dephasing coefficients that we focus on are the ones that affect the inspiral phase, namely $\delta\chi_i$. For a better display of the results, we do not plot all the energy versus time graph for all $\delta\chi_i$. Instead, we plot two graphs of energy versus time, one that corresponds to a low PN order and one that corresponds to a high PN order. Here, we choose $\delta\chi_1$ which corresponds to 0.5 PN order, and $\delta\chi_7$ which corresponds to 3.5 PN order.

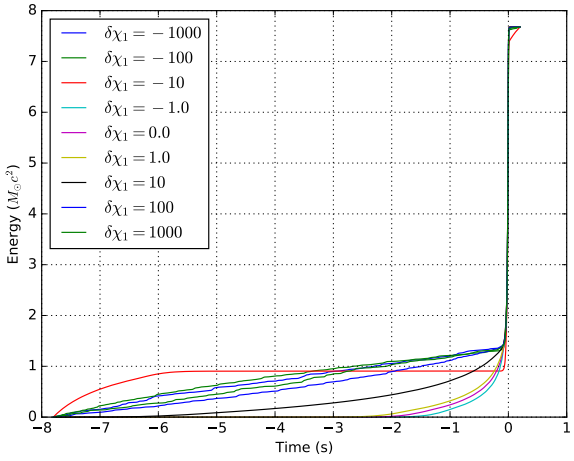

FIG. 9. Total energy of GW versus time with $m_1 = m_2 = 60$ $M_\odot$, no spin, and varying $\delta\chi_1$.

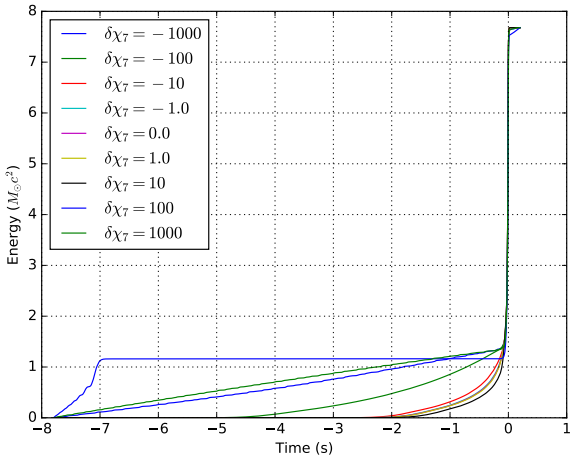

FIG. 10. Total energy of GW versus time with $m_1 = m_2 = 60$ $M_\odot$, no spin, and varying $\delta\chi_7$.

As shown in FIG. 9 and FIG. 10, the radiated energy has little to no change in the merger-ringdown phase, but has a noticeable change in the inspiral and intermediate phase. This is expected as the $\delta\chi_i$ dephasing coefficients are associated with the inspiral phase. For a visualization of the change in energy during the inspiral phase, we can plot FIG. 9 and FIG. 10 in logarithmic scale.

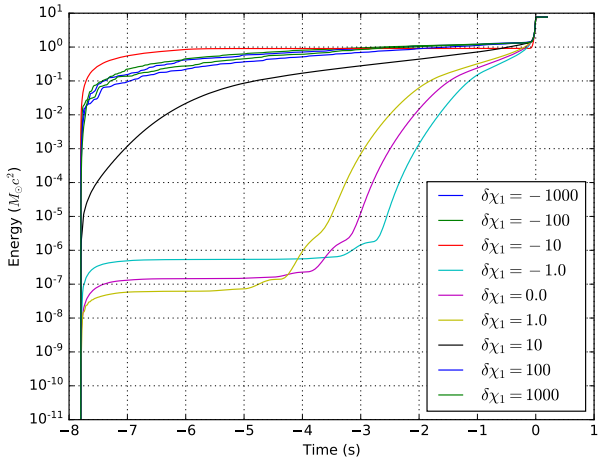

FIG. 11. Total energy of GW versus time with $m_1 = m_2 = 60$ $M_\odot$, no spin, and varying $\delta\chi_1$ in logarithmic scale.

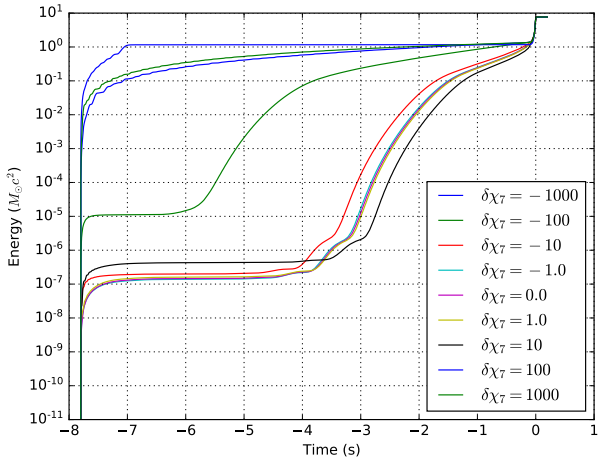

FIG. 12. Total energy of GW versus time with $m_1 = m_2 = 60$ $M_\odot$, no spin, and varying $\delta\chi_7$ in logarithmic scale.

From FIG. 11 and FIG. 12, we can see a general trend that the higher the dephasing coefficient, the higher the energy during the inspiral phase. Moreover, notice the line for $|\delta\chi_1| = 1$ and $|\delta\chi_7| = 1$, we can see that there is a larger deviation from the GR-predicted waveform for $|\delta\chi_1| = 1$. This implies that when the dephasing coefficient varies, the higher the PN order, the smaller the deviation from the GR-predicted waveform. Again, the

large deviations in dephasing coefficients have been ruled out by observation [1, 14, 20], and the sole purpose of plotting them is to better visualize the change in energy.

IV. ANALYSIS AND DISCUSSION

For a quantitative relation between intrinsic parameters and the energy, we plot the total energy versus the intrinsic parameters.

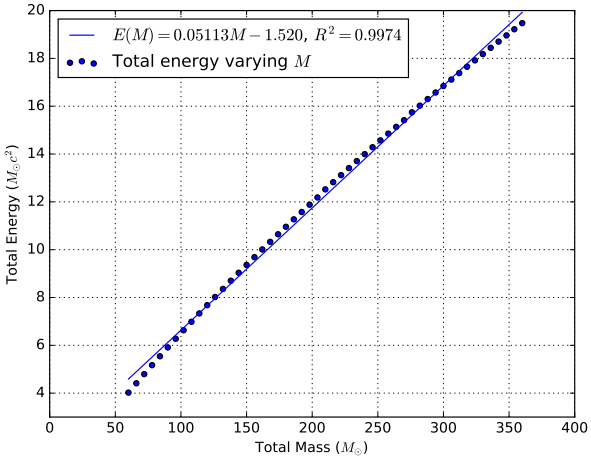

FIG. 13. Total energy of GW versus total mass with constant mass ratio $q = 1.0$ and no spin. The dots represent the total energy obtained using the numerical calculations in Section III, and the line represent the line of best fit through linear regression.

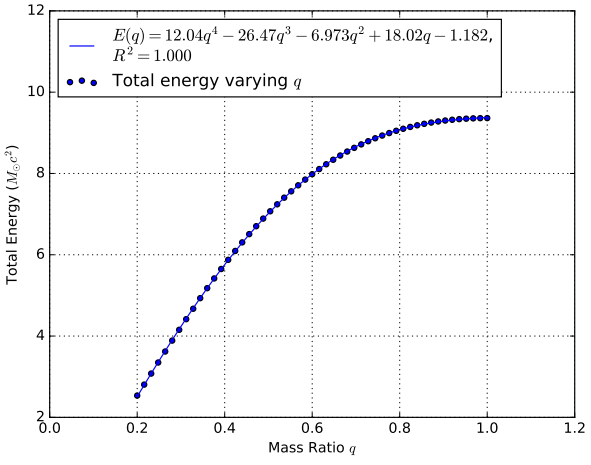

FIG. 14. Total energy of GW versus mass ratio with constant total mass and no spin in linear scale. The dots represent the total energy obtained using the numerical calculations in Section III, and the line represent the line of best fit through polynomial regression.

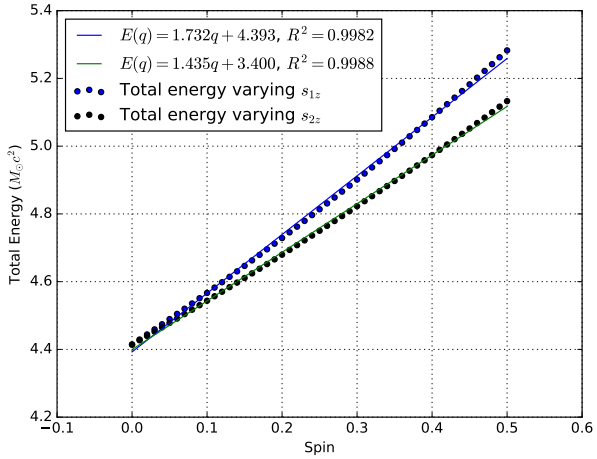

FIG. 15. Total energy of GW versus spin with $m_1 = 35.0\ M_\odot$ and $m_2 = 31.5\ M_\odot$. The dots represent the total energy obtained using the numerical calculations in Section III, and the line represent the line of best fit through polynomial regression.

As seen from FIG. 13, using linear regression, the total mass increases in a linear manner with the total energy radiated. The linear fit seems to be ideal for FIG. 13, as $R^2 = 0.9974$. On the other hand, from FIG. 14, we can see that the total energy radiated by the GW increases quartically with the mass ratio. The quartic fit seems to be ideal for FIG. 14, as $R^2 = 1.000$. However, it is important to note that the use of polynomial regression in FIG. 14, is only valid for mass ratio in the range $0.2 \leq q \leq 1.0$. This is because, as mass ratio increases, we expect the gradient of total energy versus total mass/mass ratio to decrease and get closer to zero as $q \to \infty$. However, quartic expressions only have a zero gradient at a maxima or minima. Therefore, it is also correct to say that the quartic expressions in FIG. 14 are only the best fit lines for the given data. If one were to extrapolate, one would have to plot the new points and repeat the polynomial regression for the new data set. Similar to FIG. 13, FIG. 15 shows that the total energy radiated by a GW increases linearly with the spin of the BHs. The linear fit seems to be ideal, as $R^2 = 0.9984$ and $R^2 = 0.9988$ for the linear regression of s_{1z} and s_{2z} data, respectively.

Apart from the aforementioned quantitative analysis, it is important to verify whether our results make physical sense. To do so, we compare the total radiated energy with that of real GW signals. To clarify, the LIGO-Virgo-KAGRA (LVK) teams do not directly measure the energy, the calculations done by the LVK analysis team for real events are inferred using Eq. (10). Therefore, we are merely checking our calculations with the calculations done by the LVK analysis team. We can see from FIG. 3, the total energy radiated for a binary system with constant mass ratio $q = 1.0$, and total mass of $M = 60\ M_\odot$, is $\sim 3.5\ M_\odot c^2$. Comparing this to the results of GW150914, which has component masses of

$m_1 = 35.6^{+4.8}_{-3.0}\ M_\odot$ and $m_2 = 30.6^{+3.0}_{-4.4}\ M_\odot$, mass ratio of $q = 0.85^{+0.17}_{-0.17}$, and a total radiated energy of $E = 3.1^{+0.4}_{-0.4}\ M_\odot c^2$ [1]. With this, given that the results in FIG. 3 yields a mass ratio, radiated energy, and total mass within the margin of error for the results of GW150914, it can be reasonably inferred that the results obtained in FIG. 3 are accurate. From FIG. 4, it is apparent that the total radiated energy of a binary system with mass ratio $q = 0.75$, and total mass 150 $M_\odot$, is $\sim 6.7\ M_\odot c^2$. This binary system is most similar to that of GW190521, where the component masses are $m_1 = 85^{+21}_{-14}\ M_\odot$ and $m_2 = 66^{+17}_{-18}\ M_\odot$, the mass ratio is $q = 0.78^{+0.36}_{-0.32}$, and the total radiated energy is $E = 7.6^{+2.2}_{-1.9}\ M_\odot c^2$ [10]. Again, one can infer that the results in FIG. 4 are accurate, as the mass ratio, total mass, and radiated energy are within the margin of error for the results of GW190521. For FIG. 5, we compare the results to that of an improved analysis on GW150914 with a fully spin-precessing waveform model [31]. In this analysis, the total mass, mass ratio, and radiated energies are the same as GW150914, but the spin associated with the primary and secondary masses are $s_{1z} = 0.26^{+0.52}_{-0.24}$ and $s_{2z} = 0.32^{+0.54}_{-0.29}$, respectively [31]. From FIG. 5, we can see that a binary system with $m_1 = 35.0\ M_\odot$, $m_2 = 31.5\ M_\odot$, $s_{1z} = 0.30$, and $s_{2z} = 0.30$, yields a total radiated energy of $\sim 4.6\ M_\odot c^2$. With this, it is apparent that the results from FIG. 5 agrees with the results obtained from Ref. [31], as the component masses, spins, and total energy are within the margin of error. Overall, the results seem to make physical sense, as they conform to the data gathered from observations.

Now we turn our attention to varying the dephasing coefficients. In FIG. 13-15, we chose to plot the total radiated energy versus the intrinsic parameter, as the goal is to see how the total energy evolved in time with varying intrinsic parameters. However, from FIG. 11 and FIG. 12, we can see that it is not sensible to plot the total radiated energy versus the dephasing coefficients. This is because, the total radiated energy (the peak energy of the waveform) in the merger-ringdown regime has very small variations when varying $\delta\chi_i$, which make sense as $\delta\chi_i$ only affects the waveform in the inspiral phase. This small variation will lead to complications in later stages, as it is hard to bound $\delta\chi_i$ using small variations in physical parameters. Therefore the more sensible approach to bound $\delta\chi_i$ by the energy, is to plot the peak energy during the inspiral phase. To do so, we restrict the radiated energies to those in the region of time $t \leq -3.00$ s. However, the restricted region of time $t \leq -3.00$ is exclusive to the case where $m_1 = m_2 = 60\ M_\odot$, $q = 1.00$, and $s_{1z} = s_{2z} = 0$. For different set of intrinsic parameters, one would have to change this time restriction such that the variation in energy is sufficiently large. To illustrate how the PN order affects the total energy of the GW during the inspiral phase, we plot the energy versus $\delta\chi_1$ and $\delta\chi_7$ as examples. For better visualization of the results, we plot the peak energy of the GW during the inspiral phase versus $\delta\chi_i$ in logarithmic scale, as in logarithmic scale, there is a large variation in energy when changing $\delta\chi_i$ during the inspiral phase.

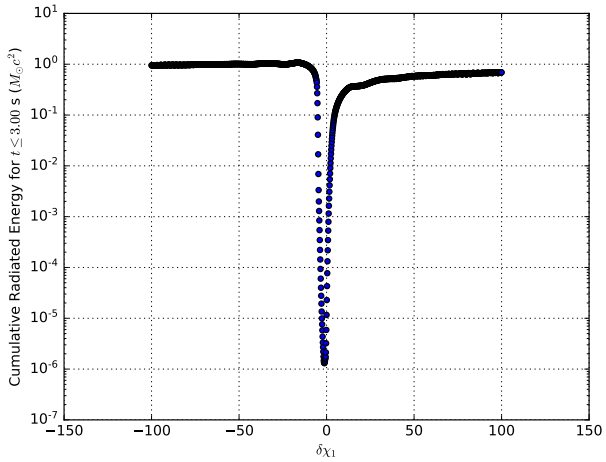

FIG. 16. Cumulative radiated energy of GW for times $t < -3.00$ s versus $\delta\chi_1$ with $m_1 = m_2 = 60\ M_\odot$ and no spin in logarithmic scale.

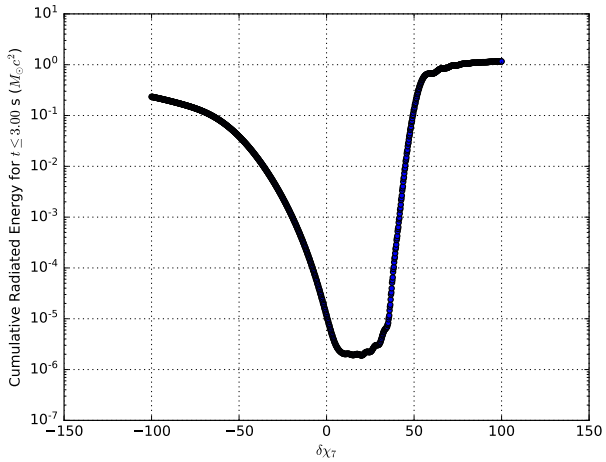

FIG. 17. Cumulative radiated energy of GW for times $t < -3.00$ s versus $\delta\chi_7$ with $m_1 = m_2 = 60\ M_\odot$ and no spin in logarithmic scale.

As seen in FIG. 16 and FIG. 17, for both low and high PN order, respectively, the radiated energy during the inspiral phase roughly increases with the absolute value of the dephasing coefficient, namely $|\delta\chi_i|$. The word roughly is used because, the minima of the distributions in FIG. 16 and FIG. 17 are not centered at $\delta\chi_i = 0$, and there is an oscillatory behavior for higher values of $\delta\chi_i$ in both 16 and FIG. 17. However, despite the fact that both graphs in FIG. 16 and FIG. 17 increase with the $|\delta\chi_1|$ and $|\delta\chi_7|$, the rate in which energy increases with

the dephasing coefficient is very different. In FIG. 16, the distribution for the energy versus $\delta\chi_1$ graph has a narrower width and has a sharper peak for when the dephasing coefficient deviates from the GR value, namely $\delta\chi_1 = 0.0$. Conversely, in FIG. 17, we can see that the cumulative radiated energy during the times $t \leq -3.00$ s increases more gradually with the dephasing coefficient than that in FIG. 16, as the shape of the distribution has a broader width. This implies that dephasing coefficients which correspond to a lower PN order are more sensitive to changes in radiated energy, as a small change in the dephasing coefficient corresponds to a large change in energy. On the other hand, dephasing coefficients that correspond to high PN orders are less sensitive to changes in radiated energy, as the change in energy with the dephasing coefficient is more moderate.

V. FUTURE WORK

By varying the intrinsic parameters and the dephasing coefficients corresponding to the inspiral part, we saw how such variation affects the evolution of energy over time. In the future, we will focus on extending similar analyses provided in this paper to the intermediate and merger-ringdown phases. In other words we vary $\delta\alpha_i$ and $\delta\beta_i$ and see how variation in these dephasing coefficient affect the evolution of energy. After this, we vary the intrinsic parameters (such as total mass, mass ratio, and spin) and the dephasing coefficients to see how they affect the evolution of angular momentum. From there, we plan to use these physical quantities, namely energy, and angular momentum, along with the GMM to coherently constrain the dephasing parameters.

VI. ACKNOWLEDGEMENT

This research has made use of data, software, and/or web tools obtained from the Gravitational Wave Open Science Center (`https://www.gw-openscience.org`), a service of LIGO Laboratory, the LIGO Scientific Collaboration, and the Virgo Collaboration. LIGO is funded by the U.S. National Science Foundation. Virgo is funded by the French Centre National de Recherche Scientifique (CNRS), the Italian Istituto Nazionale della Fisica Nucleare (INFN), and the Dutch Nikhef, with contributions by Polish and Hungarian institutes. The authors acknowledge the generous support from the National Science Foundation in the United States.

VII. APPENDIX

A. Appendix A: The Frequency Dependence of `IMRPhenomPv2`

TABLE I. The frequency dependence of `IMRPhenomPv2` dephasing coefficients used in parameterized tests of GR. The table is reproduced from TABLE I of Ref. [32].

Stage of Coalescence	Dephasing Coefficient (δp_i)	Frequency (f) Dependence
Inspiral	$\delta\chi_0$	$f^{-\frac{5}{3}}$
Inspiral	$\delta\chi_1$	$f^{-\frac{4}{3}}$
Inspiral	$\delta\chi_2$	f^{-1}
Inspiral	$\delta\chi_3$	$f^{-\frac{2}{3}}$
Inspiral	$\delta\chi_4$	$f^{-\frac{1}{3}}$
Inspiral	$\delta\chi_{5l}$	$\ln(f)$
Inspiral	$\delta\chi_6$	$f^{\frac{1}{3}}$
Inspiral	$\delta\chi_{6l}$	$f^{\frac{1}{3}}\ln(f)$
Inspiral	$\delta\chi_7$	$f^{\frac{2}{3}}$
Intermediate	$\delta\beta_2$	$\ln(f)$
Intermediate	$\delta\beta_3$	f^{-3}
Merger-Ringdown	$\delta\alpha_2$	f^{-1}
Merger-Ringdown	$\delta\alpha_3$	$f^{\frac{3}{4}}$
Merger-Ringdown	$\delta\alpha_4$	$\arctan(af+b)$

B. Appendix B: IMR Waveforms for BBHs with Non-Precessing Spins

The analytical waveform for BBHs with non-precessing spin in the frequency domain, can be written as follows [20],

$$h(f) = A(f)\cdot e^{-i\Phi(f)}, \tag{26}$$

where

$$A(f) = \mathcal{C} f_1^{-\frac{7}{6}} \begin{cases} f'^{7/6}\left(1+\sum_{i=2}^{3}\alpha_i v^i\right), & \text{if } f < f_1 \\ w_m f'^{-\frac{2}{3}}\left(1+\sum_{i=1}^{2}\epsilon_i v^i\right) & \text{if } f_1 \leq f < f_2 \\ w_r \mathcal{L}(f, f_2, \sigma) & \text{if } f_2 \leq f < 3, \end{cases} \tag{27}$$

and

$$\Psi(f) = 2\pi f t_0 + \varphi_0 + \frac{3}{128\eta v^5}\left(1+\sum_{k=2}^{7} v^k \psi_k\right). \tag{28}$$

In Eq. (27) and Eq. (28), $f' = \frac{f}{f_1}$, $v = (\pi M f)^{\frac{1}{3}}$, $\epsilon_1 = 14547\chi - 1.8897$, $\epsilon_2 = -1.8153\chi + 1.6557$, $\mathcal{C}$ is a constant that depends on the sky-location, orientation and the component masses, $\alpha_2 = -\frac{323}{224} + \frac{451}{168}\eta$ and $\alpha_3 = \left(\frac{27}{8} - \frac{11}{16}\eta\right)\chi$ are the PN corrections to the amplitude of the Fourier domain for modes $l = 2$, $m = \pm 2$ [33], t_0 is the time of arrival of the signal at the detector and ρ_0 is the corresponding phase, $\mathcal{L}(f, f_2, \sigma)$ is the Lorentzian function with width σ centered around frequency f_2, w_m

TABLE II. Phenomenological parameters describing the analytical waveforms. In test-mass limit, they reduce to the appropriate quantities given by perturbative calculations [33–35]. The test-mass limit of f_1 is a fit to the frequency of the last stable orbit [34].

	Test-mass limit (ψ_k^0)	$x^{(10)}$	$x^{(11)}$	$x^{(12)}$	$x^{(20)}$	$x^{(21)}$	$x^{(30)}$
ψ_2	$\frac{3715}{756}$	-920.9	429.1	135	6742	-1053	-1.34×10^4
ψ_3	$-16\pi+\frac{113}{3}\chi$	1.702×10^4	-9566	2182	-1.214×10^5	2.075×10^4	2.386×10^5
ψ_4	$\frac{15293365}{508032}-\frac{405}{8}\chi^2$	-1.254×10^5	7.507×10^4	1.338×10^4	8.735×10^5	-1.657×10^5	-1.694×10^6
ψ_6	0	-8.898×10^5	6.31×10^5	5.068×10^4	5.981×10^6	-1.415×10^6	-1.128×10^7
ψ_7	0	8.696×10^5	-6.71×10^5	-3.008×10^4	-5.838×10^6	1.514×10^6	1.089×10^7
	Test-mass limit (μ_k^0)	$y^{(10)}$	$y^{(11)}$	$y^{(12)}$	$y^{(20)}$	$y^{(21)}$	$y^{(30)}$
f_1	$1-4.455(1-\chi)^{0.217}+3.521(1-\chi)^{0.26}$	0.6437	0.827	-0.2706	-0.05822	-3.935	-7.092
f_2	$\frac{1}{2}\left[1-0.63(1-\chi)^{0.3}\right]$	0.1469	-0.1228	-0.02609	-0.0249	0.1701	2.325
σ	$\frac{1}{4}[1-0.63(1-\chi)^{0.3}](1-\chi)^{0.45}$	-0.4098	-0.03523	0.1008	1.829	-0.02017	-2.87
f_3	$0.3236+0.04894\chi+0.01346\chi^2$	-0.1331	-0.08172	0.1451	-0.2714	0.1279	4.922

and w_r are the normalization constants which are selected such that $A(f)$ is continuous across the transition frequencies f_2 and f_1, and f_3 is a cutoff frequency such that the signal power above f_3 is negligible. The phenomenological parameter ψ_k and $\mu_k = \{f_1, f_2, \sigma, f_3\}$ can be written in terms of the physical parameters of the binary

$$\psi_k = \psi_k^0 + \sum_{i=1}^{3}\sum_{j=0}^{N} x_k^{ij}\eta^i\chi^j, \tag{29}$$

$$\pi M\mu_k = \mu_k^0 \sum_{i=1}^{3}\sum_{j=0}^{N} y_k^{ij}\eta^i\chi^j, \tag{30}$$

where $N = \min(3-i, 2)$ while $x^{(ij)}$ and $y^{(ij)}$ are tabulated in TABLE II. It is important to note that the results in TABLE II are not originally produced by the authors of this paper, but instead reproduced from Ref. [20]. For further details of IMR waveforms for BBHs with non-precessing spins, please refer to the original paper in Ref. [20].

[1] B. P. Abbott *et al.* (LIGO Scientific Collaboration and Virgo Collaboration), Observation of gravitational waves from a binary black hole merger, Phys. Rev. Lett. **116**, 061102 (2016).

[2] B. P. Abbott *et al.* (LIGO Scientific Collaboration and Virgo Collaboration), GW151226: Observation of gravitational waves from a 22-solar-mass binary black hole coalescence, Phys. Rev. Lett. **116**, 241103 (2016).

[3] B. P. Abbott *et al.* (LIGO Scientific and Virgo Collaboration), GW170104: Observation of a 50-solar-mass binary black hole coalescence at redshift 0.2, Phys. Rev. Lett. **118**, 221101 (2017).

[4] B. P. Abbott *et al.*, GW170608: Observation of a 19 solar-mass binary black hole coalescence, The Astrophysical Journal **851**, L35 (2017).

[5] B. P. Abbott *et al.* (LIGO Scientific Collaboration and Virgo Collaboration), GW170814: A three-detector observation of gravitational waves from a binary black hole coalescence, Phys. Rev. Lett. **119**, 141101 (2017).

[6] B. P. Abbott *et al.* (LIGO Scientific Collaboration and Virgo Collaboration), GW170817: Observation of gravitational waves from a binary neutron star inspiral, Phys. Rev. Lett. **119**, 161101 (2017).

[7] B. P. Abbott *et al.* (LIGO Scientific Collaboration and Virgo Collaboration), GWTC-1: A gravitational-wave transient catalog of compact binary mergers observed by ligo and virgo during the first and second observing runs, Phys. Rev. X **9**, 031040 (2019).

[8] R. Abbott *et al.* (LIGO Scientific Collaboration and Virgo Collaboration), GW190412: Observation of a binary-black-hole coalescence with asymmetric masses, Phys. Rev. D **102**, 043015 (2020).

[9] B. P. Abbott *et al.*, GW190425: Observation of a compact binary coalescence with total mass ~ 3.4 m $\odot$, The Astrophysical Journal **892**, L3 (2020).

[10] R. Abbott *et al.* (LIGO Scientific Collaboration and Virgo Collaboration), GW190521: A binary black hole merger with a total mass of 150 $M_\odot$, Phys. Rev. Lett. **125**, 101102 (2020).

[11] R. Abbott *et al.*, GW190814: Gravitational waves from the coalescence of a 23 solar mass black hole with a 2.6 solar mass compact object, The Astrophysical Journal **896**, L44 (2020).

[12] K. S. Stelle, Renormalization of higher-derivative quantum gravity, Phys. Rev. D **16**, 953 (1977).

[13] J. Meidam, K. W. Tsang, J. Goldstein, M. Agathos, A. Ghosh, C.-J. Haster, V. Raymond, A. Samajdar, P. Schmidt, R. Smith, K. Blackburn, W. Del Pozzo, S. E. Field, T. Li, M. Pürrer, C. Van Den Broeck, J. Veitch, and S. Vitale, Parametrized tests of the strong-field dynamics of general relativity using gravitational wave signals from coalescing binary black holes: Fast likelihood calculations and sensitivity of the method, Phys. Rev. D **97**, 044033 (2018).

[14] S. Khan, S. Husa, M. Hannam, F. Ohme, M. Pürrer, X. J. Forteza, and A. Bohé, Frequency-domain gravitational waves from nonprecessing black-hole binaries. ii. a

phenomenological model for the advanced detector era, Phys. Rev. D **93**, 044007 (2016).
[15] S. Khan, K. Chatziioannou, M. Hannam, and F. Ohme, Phenomenological model for the gravitational-wave signal from precessing binary black holes with two-spin effects, Phys. Rev. D **100**, 024059 (2019).
[16] M. Hannam, P. Schmidt, A. Bohé, L. Haegel, S. Husa, F. Ohme, G. Pratten, and M. Pürrer, Simple model of complete precessing black-hole-binary gravitational waveforms, Phys. Rev. Lett. **113**, 151101 (2014).
[17] S. Husa, S. Khan, M. Hannam, M. Pürrer, F. Ohme, X. J. Forteza, and A. Bohé, Frequency-domain gravitational waves from nonprecessing black-hole binaries. i. new numerical waveforms and anatomy of the signal, Phys. Rev. D **93**, 044006 (2016).
[18] T. G. F. Li, *Extracting Physics from Gravitational Waves: Testing the Strong-field Dynamics of General Relativity and Inferring the Large-scale Structure of the Universe*, Ph.D. thesis, Vrije U., Amsterdam (2013).
[19] A. Buonanno, B. R. Iyer, E. Ochsner, Y. Pan, and B. S. Sathyaprakash, Comparison of post-newtonian templates for compact binary inspiral signals in gravitational-wave detectors, Phys. Rev. D **80**, 084043 (2009).
[20] P. Ajith, M. Hannam, S. Husa, Y. Chen, B. Brügmann, N. Dorband, D. Müller, F. Ohme, D. Pollney, C. Reisswig, L. Santamaría, and J. Seiler, Inspiral-merger-ringdown waveforms for black-hole binaries with nonprecessing spins, Phys. Rev. Lett. **106**, 241101 (2011).
[21] T. G. F. Li, W. D. Pozzo, S. Vitale, C. V. D. Broeck, M. Agathos, J. Veitch, K. Grover, T. Sidery, R. Sturani, and A. Vecchio, Towards a generic test of the strong field dynamics of general relativity using compact binary coalescence: Further investigations, Journal of Physics: Conference Series **363**, 012028 (2012).
[22] M. Agathos, W. Del Pozzo, T. G. F. Li, C. Van Den Broeck, J. Veitch, and S. Vitale, Tiger: A data analysis pipeline for testing the strong-field dynamics of general relativity with gravitational wave signals from coalescing compact binaries, Phys. Rev. D **89**, 082001 (2014).
[23] R. E. Kass and A. E. Raftery, Bayes factors, Journal of the American Statistical Association **90**, 773 (1995).
[24] G. Ashton, M. Hübner, P. D. Lasky, C. Talbot, K. Ackley, S. Biscoveanu, Q. Chu, A. Divakarla, P. J. Easter, B. Goncharov, F. H. Vivanco, J. Harms, M. E. Lower, G. D. Meadors, D. Melchor, E. Payne, M. D. Pitkin, J. Powell, N. Sarin, R. J. E. Smith, and E. Thrane, Bilby: A user-friendly bayesian inference library for gravitational-wave astronomy, The Astrophysical Journal Supplement Series **241**, 27 (2019).
[25] J. Veitch and A. Vecchio, Bayesian coherent analysis of in-spiral gravitational wave signals with a detector network, Phys. Rev. D **81**, 062003 (2010).
[26] J. Veitch, V. Raymond, B. Farr, W. Farr, P. Graff, S. Vitale, B. Aylott, K. Blackburn, N. Christensen, M. Coughlin, W. Del Pozzo, F. Feroz, J. Gair, C.-J. Haster, V. Kalogera, T. Littenberg, I. Mandel, R. O'Shaughnessy, M. Pitkin, C. Rodriguez, C. Röver, T. Sidery, R. Smith, M. Van Der Sluys, A. Vecchio, W. Vousden, and L. Wade, Parameter estimation for compact binaries with ground-based gravitational-wave observations using the lalinference software library, Phys. Rev. D **91**, 042003 (2015).
[27] M. Maggiore, *Gravitational Waves: Volume 1: Theory and Experiments* (Oxford University Press, 2007).
[28] M. Ruiz, M. Alcubierre, D. Núñez, and R. Takahashi, Multiple expansions for energy and momenta carried by gravitational waves, General Relativity and Gravitation **40**, 1705 (2008).
[29] P. J. Olver, *Introduction to Partial Differential Equations* (Springer, 2013).
[30] K. E. Atkinson, *An Introduction to Numerical Analysis* (Wiley, 1989).
[31] B. P. Abbott *et al.* (LIGO Scientific Collaboration and Virgo Collaboration), Improved analysis of GW150914 using a fully spin-precessing waveform model, Phys. Rev. X **6**, 041014 (2016).
[32] B. P. Abbott *et al.* (LIGO Scientific and Virgo Collaborations), Tests of general relativity with GW150914, Phys. Rev. Lett. **116**, 221101 (2016).
[33] K. G. Arun, A. Buonanno, G. Faye, and E. Ochsner, Higher-order spin effects in the amplitude and phase of gravitational waveforms emitted by inspiraling compact binaries: Ready-to-use gravitational waveforms, Phys. Rev. D **79**, 104023 (2009).
[34] J. M. Bardeen, W. H. Press, and S. A. Teukolsky, Rotating Black Holes: Locally Nonrotating Frames, Energy Extraction, and Scalar Synchrotron Radiation, Astrophys. J. **178**, 347 (1972).
[35] F. Echeverria, Gravitational-wave measurements of the mass and angular momentum of a black hole, Phys. Rev. D **40**, 3194 (1989).